processes

MDPI

Article

Investigating the Influence of Joint Angles on Rock Mechanical Behavior of Rock Mass Using Two-Dimensional and Three-Dimensional Numerical Models

Yang Zhao [1,2], Ye Zhao [2], Zhe Zhang [2,*], Wenhai Wang [2,*], Jiaming Shu [3], Yang Chen [4], Jianguo Ning [2] and Lishuai Jiang [1]

[1] State Key Laboratory of Mining Response and Disaster Prevention and Control in Deep Coal Mines, Anhui University of Science and Technology, Huainan 232001, China; mrzhao_y@163.com (Y.Z.)
[2] College of Energy and Mining Engineering, Shandong University of Science and Technology, Qingdao 266590, China
[3] Beijing Anke Xingye Technology Co., Ltd., Beijing 100083, China
[4] Shandong Energy Group Co., Ltd., Jinan 250014, China
* Correspondence: shaum_zz@163.com (Z.Z.); wenhaiwang2020@163.com (W.W.)

Abstract: Numerical testing is an ideal testing method in the research on the mechanical behaviors of jointed rock. However, there are few systematic studies focused on the comparison between the two-dimensional (2D) and the three-dimensional (3D) simulation effects on rock mechanical behaviors, particularly those of jointed rock. In this paper, a particle flow model was established by utilizing PFC2D and PFC3D to represent the rock materials, and the rock (especially jointed rock) mechanical behaviors (uniaxial compressive strength UCS, tensile strength TS, crack initiation stress level K_σ, and the pattern of crack initiation) between 2D and 3D models were compared and analyzed. As expected, the result shows that the UCS and TS showed an increasing tendency with the increase in the joint angle (β) for both the 2D and the 3D models, and the strength of the 3D model was less than that of the 2D model under uniaxial compression but was greater than that of the 2D model under uniaxial tension. The crack initiation and K_σ of the specimens were essentially the same for the 2D and 3D models, and the tensile stresses are more concentrated than the compressive stresses before the failure of the specimen; the uniaxial tensile failure more closely approached abrupt failure than the uniaxial compression failure. The tensile cracks were often initiated at the tips of the joints for both the 2D and 3D models, but they were initiated in the middle of the joints when β was low ($\beta = 0°$ and $\beta = 15°$ in both the 2D and 3D models) under uniaxial compression and when β reached 90° under uniaxial tensile. The test results were validated and further analyzed with mathematical analysis. This study has relative referential value to experiments on jointed rock and to analysis of the instability fractures of engineering rock mass.

Keywords: jointed rock; uniaxial compression; uniaxial tension; mechanical behavior

Citation: Zhao, Y.; Zhao, Y.; Zhang, Z.; Wang, W.; Shu, J.; Chen, Y.; Ning, J.; Jiang, L. Investigating the Influence of Joint Angles on Rock Mechanical Behavior of Rock Mass Using Two-Dimensional and Three-Dimensional Numerical Models. *Processes* **2023**, *11*, 1407. https://doi.org/10.3390/pr11051407

Academic Editor: Yong Yuan

Received: 27 March 2023
Revised: 27 April 2023
Accepted: 30 April 2023
Published: 6 May 2023

1. Introduction

A laboratory test is an important means of gaining a good understanding of rock strength and deformation, which is beneficial to the cost-effective design and long-term stability maintenance of engineering structures constructed in rocks or on rocks. Most rocks in actual engineering are under compression, and there has been broad research concerned with the mechanical behaviors of rocks under a compression load [1–3]. On the other hand, due to the much smaller tensile strength of rocks as compared to their compressive strength, tensile failure is the main and significant failure mode of rocks [4,5]. Consequently, the study of mechanical behaviors of rocks under tensile load has been equally important. However, the laboratory tests are affected by the significant amount of time required, especially for jointed rock, which is difficult to prepare. In addition, it remains a considerable challenge

to conduct direct uniaxial tensile tests on intact rock specimens in laboratories due to the difficulty in gripping the rock specimens and to misalignment [1,3].

Based on the above situations, numerical testing is undoubtedly a more ideal testing method in the research on the mechanical behaviors of jointed rock than the other methods. There are generally two types of numerical methods available: the continuum method and the discontinuum method. The continuum-based method uses an average measure of material degradation to represent the microscale damage in a constitutive relation. In the discontinuum method, the material is directly idealized as an assembly of separate units, such as blocks or particles, bonded together at their contact points, and the internal damage is represented by the breakage of the bonds [6]. In addition, rock is a typically discontinuous and heterogeneous material; so discontinuum-based methods have been increasingly used to simulate the mechanical behaviors of rocks [7]. For example, Wu et al. [8] used the discontinuum method based on the block discrete element model to analyze the influence of the parameters of the joint network on the mechanical property and failure mode of jointed rock. Another discontinuum method, based on the particle flow program, was used by Tong et al. [9] to investigate the mechanical response before and after chemical corrosion.

One of the popularly used discontinuum methods is the discrete element method (DEM), which is commonly adopted to simulate the microcrack initiation, propagation, and coalescence associated with the rock failure processes [7,10]. In addition, a widely used example of the DEM approach is the particle flow code (PFC), based on the bonded particle model (BPM); in this case, the bond is simply broken when the interaction force between two particles overcomes its tensile or shear strength, and the microcrack is produced automatically without further assumptions about where and how the cracks may appear [11]. This method is widely used for the analysis of the characteristics and changes in the rock microstructure, the distribution and transmission of internal stress, the generation and development of damage cracks, etc. (a study on the cracking behavior of asphalt mixture by discrete element modeling with real aggregate morphology). The flat-joint model (FJM) analysis was proposed by Potyondy [12] in 2012 and was implemented in both PFC2D and PFC3D by Itasca in 2015; this model was capable of reproducing the expected high uniaxial compressive strength to tensile strength ratio (UCS/TS) and the internal friction angle and even to derive a nonlinear strength envelope [13]. The improved model has been validated and widely used for rock or rock-like materials. For example, a careful examination of the mechanical behavior of the flat-joint contact and a systematic calibration was conducted by Cheng et al. [14] to build some numerical models matching the mechanical properties of Carrara marble, and the results suggest that the FJM is capable of matching both the mechanical properties and the fracturing behavior of Carrara marble. Yang et al. [13] used FJM to study the mechanical behavior of granite materials containing discontinuous joints and found that the joint persistency and UCS/TS had a pronounced effect on the failure mode, the peak shear strength, and the shear deformation modulus of the granite samples containing discontinuous joints.

Undoubtedly, from the morphological perspective, three-dimensional models provide more realistic simulations of specimens, and their effects are closer to those of real experiments [15,16]. However, compared to three-dimensional models, two-dimensional models of the same size are denser, the extension of the model cracks is more intuitive, and the model generation and calculation processes are faster. The discussion on the influence of dimension on simulation results is highly significant for model selection in the future analyses of rock mechanics problems. In recent years, scholars have conducted research on this topic. For example, Liu et al. [17] established two-dimensional and three-dimensional asphalt mixture models and simulated the dynamic modulus test, and the results showed that the dynamic elastic modulus and phase angle were similar in both 2D and 3D. Gao et al. [18] simulated two-dimensional and three-dimensional semi-circular bending and tensile tests, and the results demonstrated a similar failure mode and level of tensile strength in both dimensions. While these studies have confirmed the practicality and reliability of 2D simplified models in some respects, research on the mechanical behaviors

of jointed rock in different dimensions, especially the influence of the failure mode and crack initiation mechanism of jointed rock, is still limited. Natural rock formations always contain many defects and joints, and the study of crack initiation mechanisms is of great significance to future experimental research on jointed rock and even the unstable fracture analysis of engineering rock formations [19–21].

In this paper, a particle flow model was established by utilizing the PFC2D and PFC3D to represent the intact rock materials. In addition, the rock (especially the jointed rock) mechanical behaviors (UCS, TS, crack initiation stress level K_σ, and the pattern of crack initiation) between two-dimensional (2D) and three-dimensional (3D) models were compared and analyzed. Additionally, the relationship between the joint angle (β) and the specimen strength (σ_c and σ_t) was confirmed by mathematical calculations. This study reveals the influence of the regularity of rock mechanical behaviors on the joint angle in PFC2D and PFC3D, and it has a relative referential value to the choice of model of numerical experimentation. In addition, the study of the crack initiation mechanism is significantly important to the experiment on jointed rock and the analysis of the instability fracture of the engineering rock mass.

2. Numerical Model and Mechanical Behaviors of Intact Specimen

2.1. Calibration of Model Parameters

The FJM, which conforms to the actual UCS/TS of rock, was utilized for PFC2D and PFC3D simulations. Rectangular specimens with a height of 100 mm and a width of 50 mm and cylindrical specimens with a height of 100 mm and a diameter of 50 mm were created in the 2D and 3D models, respectively. The loading rate applied during calibration was 0.05 m/s and 0.0025 m/s for the compression and direct tension tests, respectively [22,23].

The random seed was set to 10,001 in the numerical model. In addition, the 2D model consisted of uniformly distributed particles, with the radius ranging from 0.26 mm ($R_{\min}$) to 0.39 mm ($R_{\max}$); the 3D model consisted of uniformly distributed particles, with the radius ranging from 0.80 mm ($R_{\min}$) to 1.60 mm ($R_{\max}$) [24,25]. The joints were set using a direct particle deletion method. Finally, each model contained about 14,698 particles and 36,468 contacts in the 2D model and about 45,889 particles and 261,754 contacts in the 3D model; this varied slightly among the different joint sets.

The micro-properties obtained through the trial and error methods in this study are listed in Table 1. These parameters were utilized to match the actual response of coal specimens by comparing them with the material parameters, focusing specifically on comparing the uniaxial compressive strength (UCS), uniaxial compressive elastic modulus (E_c), uniaxial tension elastic modulus (E_t), tension strength (TS), and the ratio of UCS to TS. The calibration of the microparameters for the 2D and 3D models, despite being based on the same macroscopic mechanical properties, still resulted in differences due to the distinct mechanical behaviors of both models when subjected to loads.

Figure 1a shows the stress–strain curves of the numerical model (2D and 3D) and the coal specimen (black coal, taken from the roof of the Hongqinghe mine, China) under uniaxial compression, and Figure 1b shows the stress–strain curves of the 2D model and the 3D model under uniaxial tension. It can be seen that the 2D model and the 3D model can both match well with the mechanical property of the coal specimen under uniaxial compression. In addition, the stress–strain curves of the 2D model and the 3D model show good agreement with each other, in terms of both uniaxial compression and uniaxial tension. The mechanical properties were used for the calculation and the UCS/TS of the 2D and 3D models were obtained as 18.79 and 17.96, respectively; these were very consistent and conformed to the characteristics of the rock [26–28].

Table 1. Calibrated microparameters of numerical model.

Microparameter	Symbol	Value	
		2D	3D
Parameters associated with material genesis			
Particle density	ρ_s (kg/m^3)	2500	2500
Minimum particle radius	R_{min} (mm)	0.26	0.8
Particle size ratio	R_{max}/R_{min}	1.5	1.5
Particle modulus	E_p (GPa)	1.25	1.0
Particle friction coefficient	K_p	1.0	1.0
Particle friction coefficient	μ_p	0.7	0.7
Parameters associated with flat-joint contact			
Number of segments	N	5	5
Friction coefficient	M	0.53	0.58
Bond tensile strength	σ_t (MPa)	1.05	0.65
Bond cohesion	σ_c (MPa)	5.8	3.8
Friction angle	φ (°)	30	30
Modulus	E (GPa)	1.25	1.1
Stiffness ratio	K	1.3	1.3

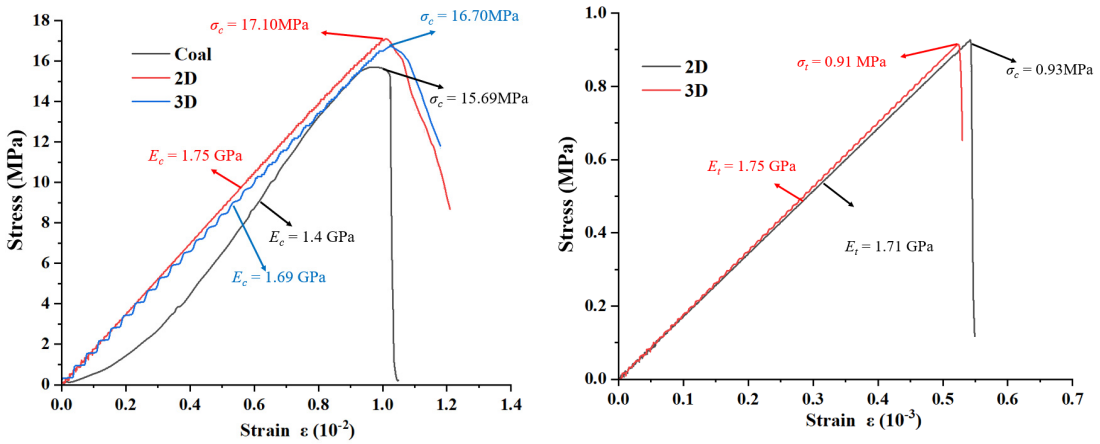

(**a**) Uniaxial compression (**b**) Uniaxial tension

Figure 1. Comparison of stress-strain curves between numerical model and coal specimens.

2.2. Analysis of Mechanical Behaviors of Intact Specimen

Zhou et al. [29] considered the fact that the crack initiation stress level can describe the difficult extent of the crack initiation for flawed specimens and can be defined by Equation (1).

$$K_\sigma = \frac{\sigma_{max} - \sigma_{ci}}{\sigma_{max}} \times 100\% \quad (1)$$

where σ_{max} is the peak strength under uniaxial compression (σ_c) or uniaxial tension (σ_t) of the specimens; σ_{ci} is the crack initiation stress; and K_σ is the crack initiation stress level.

A model that has a smaller crack initiation stress level indicates that it is difficult to crack in low stress and that the stress is more concentrated before the failure of the specimen; in contrast, a model is easier to crack when it has a larger initiation stress level. This study classified crack initiation (ECI) according to difficult initiation ($K_\sigma \leq 30\%$), medium initiation ($30\% < K_\sigma < 70\%$), and easier initiation ($K_\sigma \geq 70\%$), according to K_σ, which indicates the degree to which the specimen is easy or difficult to crack.

For intact specimens, cracks always initiate near the ends of the specimen under compressive loading, as shown in Figure 2; this applies to both the 2D and the 3D models. This may be related to the fact that the load is transferred from the ends of the specimen.

In addition, the crack initiation stress was 5.67 MPa in the 2D model and 5.18 MPa in the 3D model, with a difference of only 0.49 MPa. After calculation using Equation (1), we observed slight, but not substantial differences in K_σ and both were at the medium initiation level using these two methods (2D and 3D), with a level of 66.84% for the 2D model and 68.96% for the 3D model. In addition, since there was no obvious stress concentration zone in the intact specimen and the load transfer began at the end of the specimen, the loading process not only produced cracks through both ends of the specimen but also direct damage of the block at the end of the specimen.

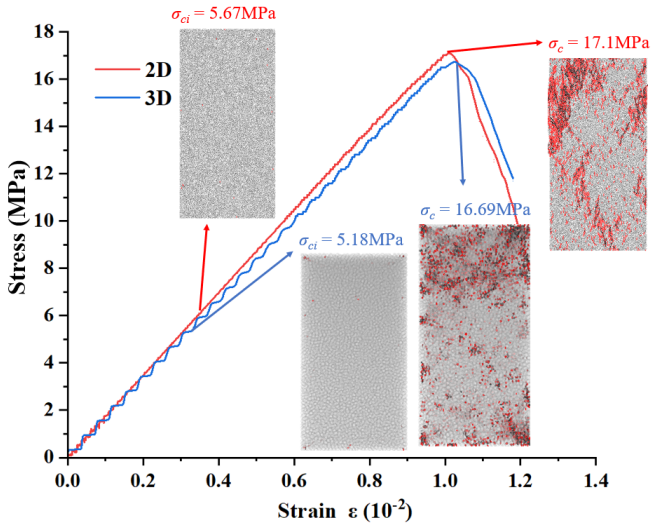

Figure 2. Crack pattern for initiation stress and peak stress under uniaxial compression.

Although the strength exhibited under uniaxial tension was much smaller than that under uniaxial compression, the crack initiation only occurred when the stress was close to the peak under tensile loading; σ_{ci} was 0.82 MPa for the 2D model and 0.80 MPa for the 3D model, while $\sigma_{\max}$ for the 2D and 3D models was 0.93 MPa and 0.91 MPa, respectively. After calculation using Equation (1), the K_σ was obtained as 11.83% for the 2D model and 12.09% for the 3D model, which were far less than those for uniaxial compression. This indicated that the tensile stresses were more concentrated than the compressive stresses before the failure of the specimen; the uniaxial tensile failure more closely approached abrupt failure than the uniaxial compression failure. Similarly, since the load was transferred from the ends of the specimen, the cracks also initiated near the ends of the specimen under tension loading, as shown in Figure 3; this applies to both the 2D and the 3D models and is consistent with the direct tensile failure of real rocks [6,30].

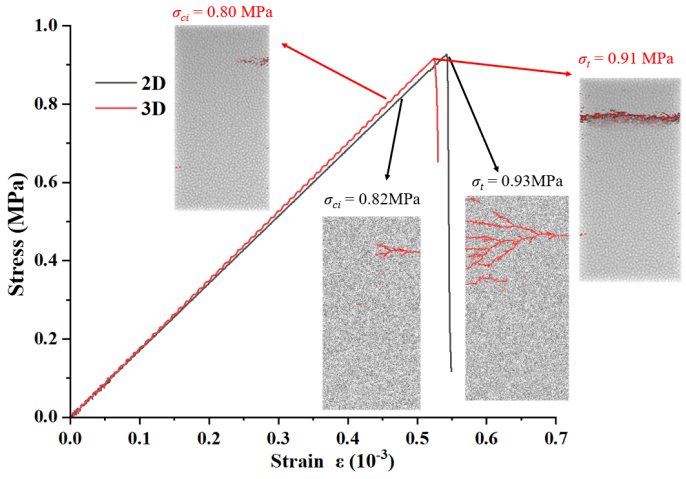

Figure 3. Crack pattern for initiation stress and peak stress under uniaxial tension.

According to the comparison of the rock mechanical behaviors of the intact specimens between the 2D and 3D models under uniaxial compression and tension, it can be seen that the crack initiation and K_σ of the specimens were essentially the same, under both uniaxial compression loading and uniaxial tensile loading. In a later section, we analyze and compare the rock mechanical behaviors (UCS, TS, and K_σ) for different joint angles between the 2D and 3D models.

3. Comparison of Rock Mechanical Behaviors between 2D and 3D Models

3.1. Analysis of Rock Mechanical Behaviors under Uniaxial Compression

3.1.1. Comparison of UCS between 2D and 3D models

According to the trend of *UCS* changing with β (Figure 4), it can be seen that the relationship between *UCS* and β had an obvious regularity both for the 2D and 3D models. The *UCS* showed an increasing tendency with the increase in β, and the lowest points all appeared when $\beta = 0°$; for the 2D and 3D models, they were 9.49 MPa and 9.10 MPa, respectively; yet, the highest points all appeared when $\beta = 90°$; for the 2D and 3D models, they were 16.71 MPa and 14.51 MPa, respectively. In addition, the difference in UCS between the 2D and 3D models increases with the increasing β. When $\beta = 0°$, the difference was only 0.39 MPa, but when β increased to 90°, the difference increased to 2.20 MPa. It can also be seen that the change in UCS was insignificant with the increase in β from 0° to 15° for both the 2D and 3D models, with rates of change of only 0.32% for the 2D model and 0.65% for the 3D model, whereas when $\beta > 15°$, it can be seen that the increase in UCS became significant, with a total rate of change of 75.52% for the 2D model and 58.53% for the 3D model with an increase in β from 15° to 90°. This indicates that as β increases, its effect on the UCS of the specimen also increases significantly.

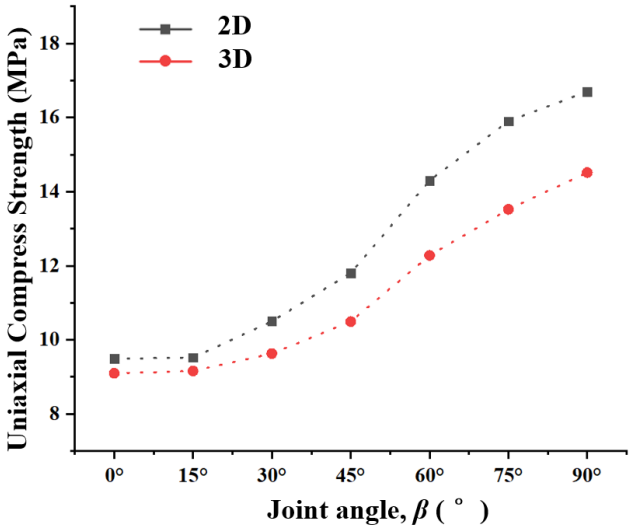

Figure 4. Comparison UCS change with β between the 2D and 3D models.

3.1.2. Comparison of Pattern and Stress of Crack Initiation between 2D and 3D Models

The K_σ with different β under uniaxial compression was calculated according to Equation (1) and is shown in Figure 5, where the ease with which the crack initiation (ECI) occurred is also divided. It can be seen that the ECI for both the 2D and 3D models behaved as if it were easier, and the change in K_σ was not significant when β was between 0° and 45°, with maximum differences of only 0.84% for the 2D model and 1.22% for the 3D model; however, when β reached 45° the change in K_σ became significant, and the maximum difference became 10.49% for the 2D model and 16.05% for the 3D model, with the increase in β from 45° to 90°. This indicates that cracking of specimens under uniaxial compression loading is relatively easy when β is small but becomes relatively difficult when β reaches 45°; this pattern was more pronounced for the 3D model.

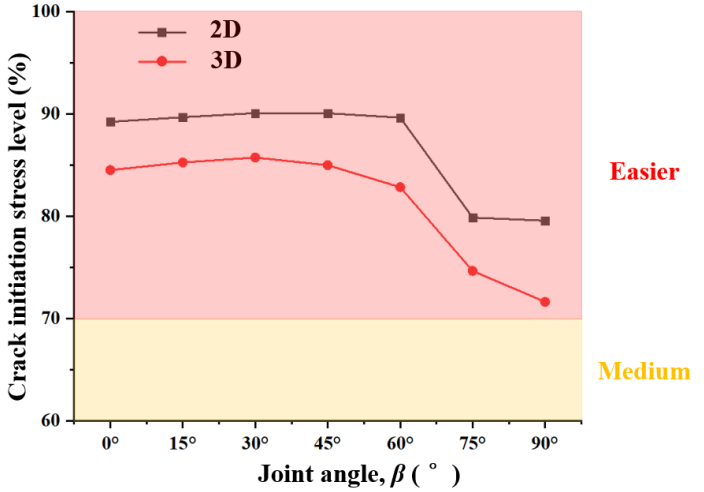

Figure 5. Comparison of K_σ change with β between the 2D and 3D models under uniaxial compression.

The failure process of the different dip angles of β was traced by PFC2D and PFC3D, as shown in Figure 6; it can be seen that the wing cracks were often initiated at the tips of the joints but were only initiated at the middle of the joint when β was low ($\beta = 0°$ and $\beta = 15°$ in both the 2D and 3D models). In addition, the propagation length of the wing crack before the microcrack appeared to decrease with the increase in β.

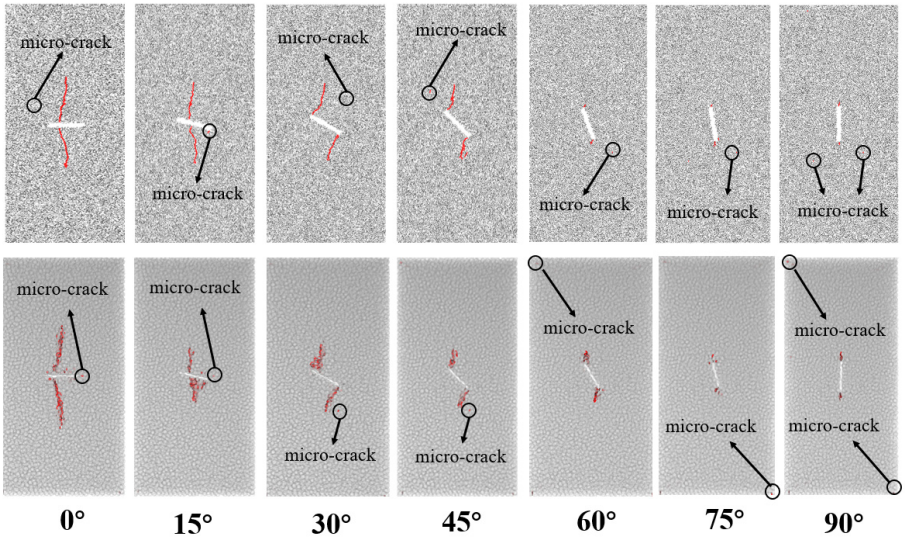

Figure 6. Crack initiation pattern with various β under uniaxial compression.

3.2. Analysis of Rock Mechanical Behaviors under Uniaxial Tension

3.2.1. Comparison of TS between 2D and 3D Models

Figure 7 shows the trend of *TS* changing with β; it can be seen that the relationship between σ_t and β had obvious regularity for both the 2D and 3D models. The σ_t showed an increasing tendency with the increase in β, and the lowest points appeared when $\beta = 15°$ for the 2D model (0.29 MPa) and when $\beta = 0°$ for the 3D model (0.31 MPa); yet, the highest points all appeared when $\beta = 90°$; for the 2D and 3D models, these were 0.93 MPa and 0.91 MPa, respectively. It should be noted that the strength of the 3D model was greater than that of the 2D model under uniaxial tension, which was different from the uniaxial compression. In addition, it can be seen that the change in TS was insignificant with the increase in β from 0° to 45° for both the 2D and 3D models, with a rate of change of only 2.33% for the 2D model and 31.96% for the 3D model, whereas when $\beta > 45°$, it can be seen that the increase in TS became significant, with a total rate of change of 157.33% for the 2D

model and 90.89% for the 3D model with the increase in β from 45° to 90°. This indicates that as β increases, its effect on the TS of the specimen also increases significantly; the same is the case for the uniaxial compression.

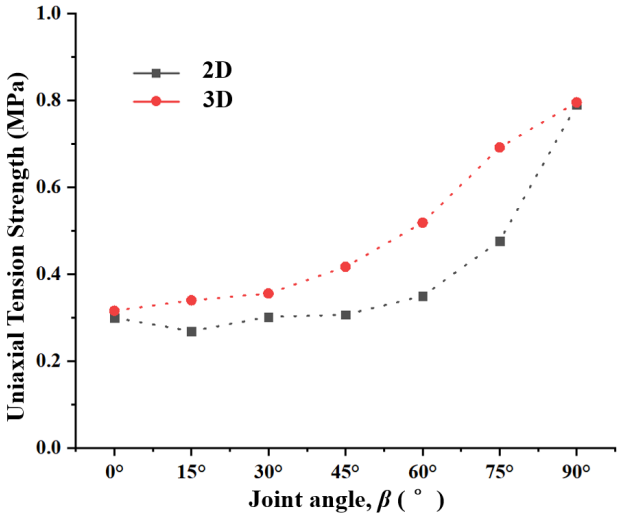

Figure 7. Comparison TS change with β between the 2D and 3D models.

3.2.2. Comparison of TS between 2D and 3D Models

The K_σ with different β under uniaxial tension was calculated according to Equation (1) and is shown in Figure 8. It can be seen that the K_σ showed a decreasing tendency with the increase in β, although the uneven distribution of particles during the setting of the fractures inevitably led to an easier initiation of cracks in the test specimen (for example, when β = 15°), but it did not have a significant impact on the determination of the overall trend. It should also be noted that the K_σ of the 3D model was greater than that of the 2D model under the uniaxial tension, which was different from the uniaxial compression. In addition, it can be seen that the ECI behaves as if it were medium when $0° \leq \beta \leq 30°$ for the 3D model; yet, the ECI behaves as if it were medium only when $\beta = 0°$ for the 2D model. This indicated that the 3D model specimens were easier to crack than the 2D model specimens under uniaxial tensile. When β reached a large value ($\beta \geq 15°$ for the 2D model, $\beta \geq 45°$ for the 3D model), the ECI of the specimen behaved as if it were difficult, especially when β = 75°, where the value of K_σ was only 2.94% for the 2D model and 15.90% for the 3D model; the stress of the crack initiation point was very close to the peak.

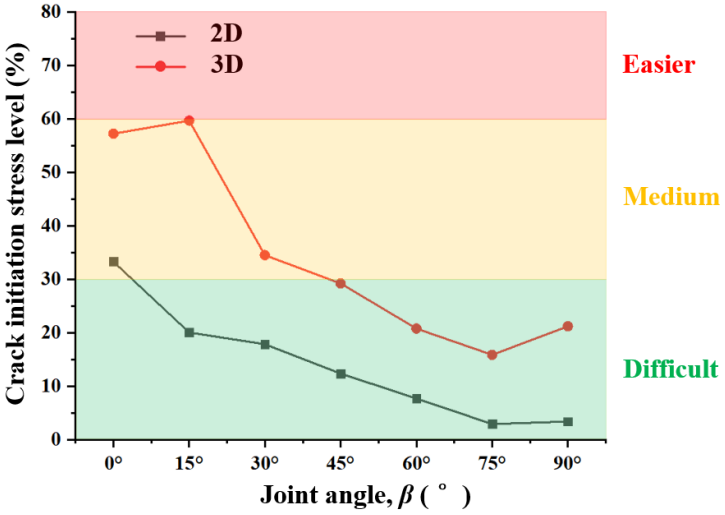

Figure 8. Comparison of K_σ change with β between the 2D and 3D models under uniaxial tension.

The crack initiation pattern under the uniaxial tension of the different dip angles of β was traced by PFC2D and PFC3D, as shown in Figure 9; it can be seen that the tensile cracks were initiated at the tips of the joints when $\beta \leq 75°$. However, when β reached 90°, the tensile cracks were initiated in the middle. Zhao et al. [3] found that samples with different openings showed similar regularity. It is noteworthy, as can be seen in Figure 9, that the crack was initiated in a non-symmetrical way at the tips of the crack in PFC2D for β = 75° and 90° and in PFC3D for 90°, which may be related to the uneven distribution of particles [4].

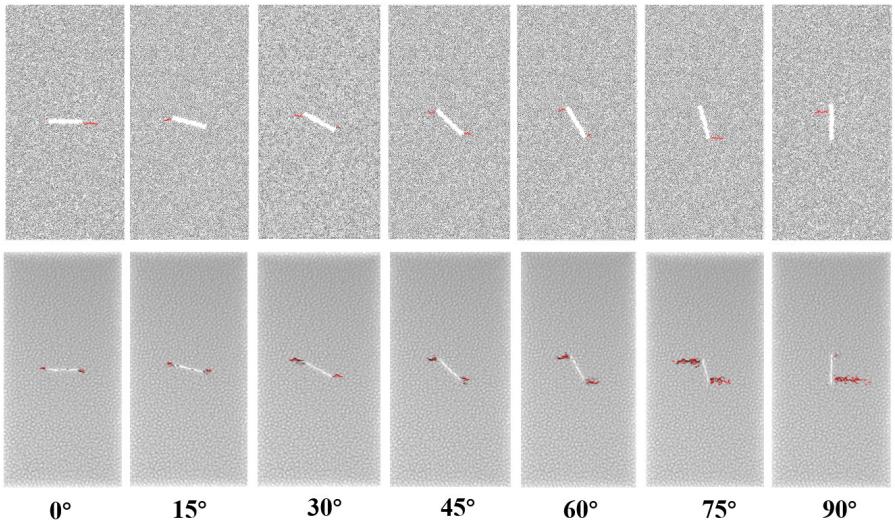

Figure 9. Crack initiation pattern with various β under uniaxial tension.

3.3. Summary

According to the above analysis, the σ_{max} showed an increasing tendency with the increase in β for both the 2D and 3D models, whether under uniaxial compression loading or under uniaxial tensile loading. In addition, it should be noted that the strength of the 3D model was less than that of the 2D model under uniaxial compression, but greater than that of the 2D model under uniaxial tension.

In addition, under both uniaxial compression loading and uniaxial tensile loading, the crack initiation and the K_σ of the specimens were essentially the same for the 2D and 3D models. Additionally, for both the 2D and 3D models, the tensile stresses were more concentrated than the compressive stresses before the failure of the specimen; the uniaxial tensile failure approached more closely to abrupt failure than the uniaxial compression failure. The tensile cracks were often initiated at the tips of the joints for both the 2D and 3D models, but the tensile cracks were initiated at the middle of the joint when β was low (β = 0° and β = 15° in both 2D and 3D models) for the uniaxial compression and when β reached 90° for the uniaxial tensile.

4. Mathematical Analysis

The relationship between the geometric parameters of the joint and the specimens can cause two-dimensional and three-dimensional analysis challenges. As shown in Figure 10, where l_1 is the horizontal projection length of l; d is the joint aperture; l_2 is the horizontal projection length of d; $l_{\min}$ is the minimum section length at which the load can be transferred on both sides of the joint under 2D conditions ($l_{\min}$ is distributed symmetrically on both sides of the joint); and $S_{\min}$ is the minimum cross-sectional area at which the load can be transferred on both sides of the joint under 3D conditions ($S_{\min}$ is distributed symmetrically on both sides of the joint).

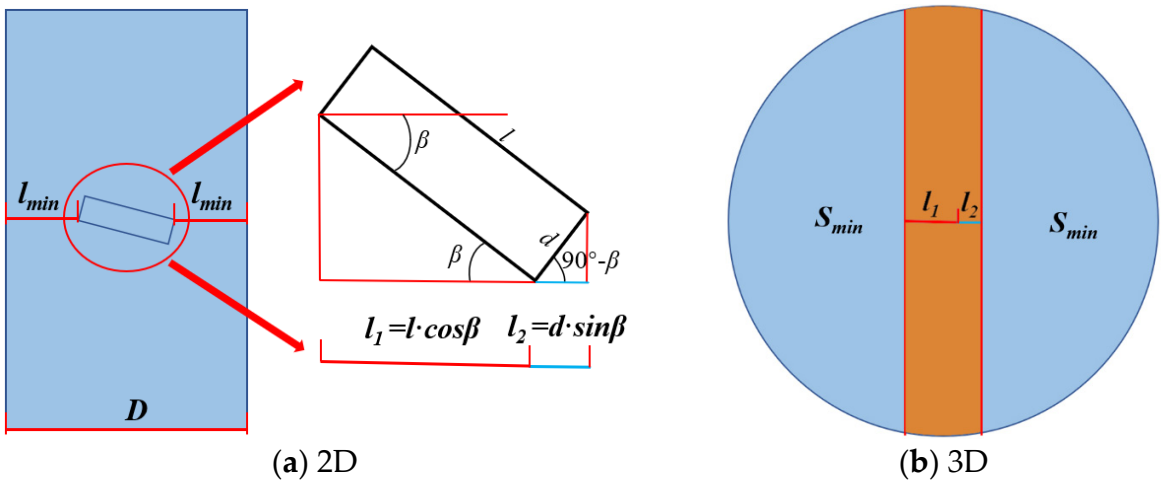

Figure 10. Feature analysis of joint space ($0° \leq \beta \leq 90°$).

According to Figure 10, l_1 and l_2 can calculated as follows:

$$l_1 = l \cdot \cos\beta \tag{2}$$

$$l_2 = d \cdot \cos(90 - \beta) = d \cdot \sin\beta \tag{3}$$

Then, $l_{\min}$ can be calculated as follows:

$$l_{\min} = \frac{D - l \cdot \cos\beta - d \cdot \sin\beta}{2} \tag{4}$$

Then, simplify the horizontal projection graph of the joint to a rectangle with a length D and a width which is the sum of l_1 and l_2. Then, $S_{\min}$ can be calculated as follows:

$$S_{\min} = \frac{\pi D^2 - D \cdot (l \cdot \cos\beta + d \cdot \sin\beta)}{2} \tag{5}$$

From Equations (4) and (5), it can be seen that $l_{\min}$ and $S_{\min}$ are inversely proportional to l and d and proportional to β when the effect of d is ignored. This means that as l and d decrease, $l_{\min}$ and $S_{\min}$ increase in proportion to β. Additionally, the uniaxial strength (including UCS and TS) of the specimen can be calculated using Equation (6) [31]:

$$\sigma = \frac{P}{A} \tag{6}$$

where σ is the uniaxial strength (including UCS and TS) of the jointed specimen; P is the peak load (including compression and tension); and A is the bottom area of the jointed specimen.

In this study, the subsequent calculation is based on the following underlying assumptions [32]:

(1) The internal material of the specimen satisfies the homogenization assumption and the isotropy assumption. This assumption suggests that the internal material of the sample can be regarded as a homogenized material with a single property and that the material is isotropic, meaning that it has the same properties in all directions.

(2) The load is uniformly transmitted inside the specimen. This assumption states that the load is distributed equally throughout the specimen. This is a commonly made assumption in structural engineering analysis as it allows for more simplified calculations.

Based on the above assumptions, the value of P is positively correlated with l_{min} and S_{min}, and the relationship of strength (including UCS and TS) between the jointed specimen and the intact specimen for the 2D and 3D models can be obtained, respectively, as follows:

$$\sigma = \frac{2l_{min}}{D}\sigma' \tag{7}$$

$$\sigma = \frac{2S_{min}}{A}\sigma' \tag{8}$$

where σ' is the strength (including UCS and TS) of the intact specimen.

According to Equations (7) and (8), as can be seen, σ is clearly positively correlated with l_{min} and S_{min}; then, Equations (4) and (5) are incorporated into Equations (7) and (8), respectively. Therefore, the relationship between the strength (including UCS and TS) of the jointed specimens when considering the change in the joint angle β and the strength of the intact specimens in the 2D and 3D models can be seen, respectively, as follows.

$$\sigma = \left(1 - \frac{l \cdot \cos\beta + d \cdot \sin\beta}{D}\right)\sigma' \tag{9}$$

$$\sigma = \left(1 - \frac{l \cdot \cos\beta + d \cdot \sin\beta}{\pi D}\right)\sigma' \tag{10}$$

From Equations (9) and (10), it is clear that when d is ignored, the parameter σ is positively correlated with β and negatively correlated with l and d. Furthermore, the relationship between σ and β in the 2D and 3D models is plotted in Figure 11, using l = 15 mm and d = 2 mm as example measurements. According to the graph, it can be seen that σ exhibits a decreasing trend initially and then increases with the β increase, regardless of the dimensionality of the system. The lowest point on the curve is reached at $\beta = 8°$, at which point the JISR values are 0.697 and 0.615, respectively. Obviously, the effect of β on σ in the 3D conditions is stronger than that in the 2D conditions. In addition, the regularities of the σ change with the β obtained from the calculation is consistent with that obtained from the numerical simulations and the experiments of the previous studies [33], as shown in Figure 11. At the same time, the comparison between the calculation and the experiment also proves that l_{min} and S_{min} are the most critical factors affecting the σ of the specimen with non-closed joints.

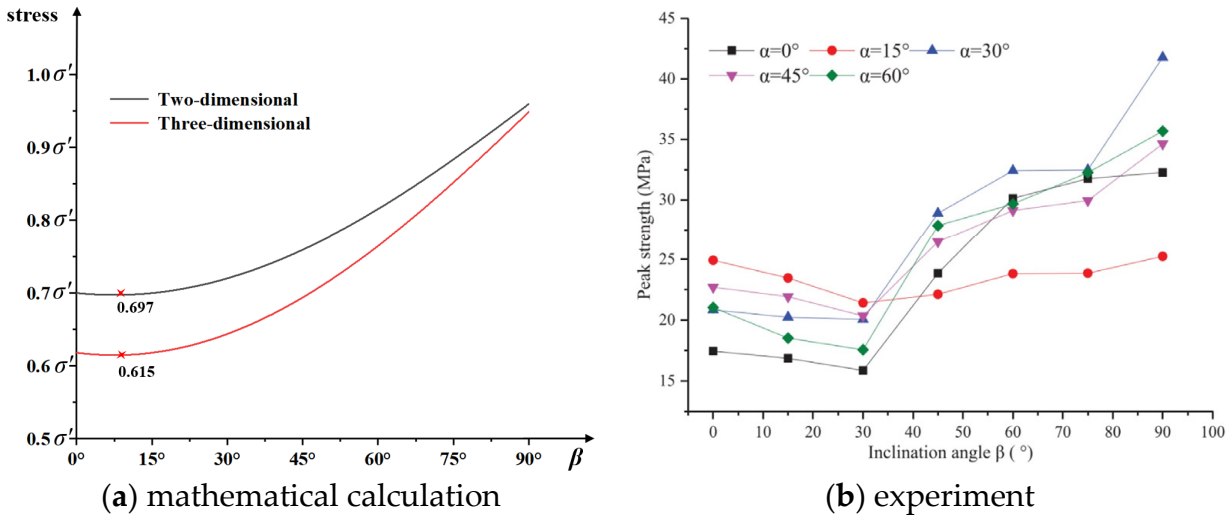

(**a**) mathematical calculation (**b**) experiment

Figure 11. The σ varies with the β [33].

5. Discussion

Mathematical calculations can verify the reliability of numerical simulations well. However, since the mathematical calculations were carried out in an ideal state, only the geometric parameters of jointed rock were considered in the analysis process. In addition, other factors might also have affected the performance, such as stress concentration, internal friction angle, heterogeneity, the uneven effect of transmitted load, etc., which were not considered in the calculations. Therefore, although the β-σ_{max} curve obtained by the mathematical calculations was consistent with the simulation results in the overall trends, the amplitudes of the σ_{max} change with β and the position of the lowest point could not completely correspond with the mathematical calculations, which should be considered in subsequent studies.

There were significant differences in the load-bearing structure of PFC2D and PFC3D, which can be seen from the ratio of the contact and ball in the model. For the intact models, the PFC2D model contained approximately 14,698 particles and 36,468 contacts, while the PFC3D model contained approximately 45,889 particles and 261,754 contacts. In the PFC2D model, the ratio of the contact to the ball was 2.48, while in the PFC3D model, it was 5.70, which was 2.30 times higher than in the PFC2D model. These differences in the load-bearing structure led to different microparameters that were calibrated based on the same macroscopic mechanical parameters.

When joints were present, the PFC2D model exhibited a more pronounced tip effect than the PFC3D model. As a result, the PFC2D specimens were more likely to crack under uniaxial compression, and the PFC2D K_σ was therefore greater than the PFC3D K_σ under uniaxial compression. However, due to the simpler load-bearing structure of the PFC2D model, especially under tension loads, this simpler structure led to a more rapid expansion of cracks in the PFC2D model. This resulted in a faster evolution of cracks in the PFC2D specimen under tension loads, leading to a significant decrease in the strength and K_σ of the PFC2D model compared to the PFC3D model. Therefore, when joints were present, the K_σ of the PFC3D specimen was greater than that of the PFC2D specimen under uniaxial tension, and the PFC3D TS was greater than that of the PFC2D TS, which led to significant differences in the numerical simulation results of the uniaxial tension of the specimens with joints in the 2D state compared to the mathematical analysis results.

6. Conclusions

In the present paper, a particle flow model was established by utilizing the PFC2D and PFC3D to represent the intact rock materials. In addition, the rock (especially the jointed rock) mechanical behaviors (UCS, TS, K_σ, and the pattern of crack initiation) between two-dimensional (2D) and three-dimensional (3D) models were compared and analyzed. Additionally, the relationship between the joint angle (β) and the specimen strength (σ_c and σ_t) was confirmed by mathematical calculations. According to the above analysis, the following conclusions can be drawn:

(i) Whether it was under uniaxial compression loading or under uniaxial tensile loading, the σ_c showed an increasing tendency with the increase in β for both the 2D and 3D models, which was consistent with the result of mathematical calculations. In addition, the strength of the 3D model was less than that of the 2D model under uniaxial compression but greater than that of the 2D model under uniaxial tension.

(ii) Under both uniaxial compression loading and uniaxial tensile loading, the crack initiation and K_σ of the specimens was essentially the same for the 2D and 3D models. In addition, for both the 2D and 3D models, the tensile stresses were more concentrated than the compressive stresses before the failure of the specimen; the uniaxial tensile failure approached more closely to abrupt failure than the uniaxial compression failure.

(iii) For the 2D and 3D models, the tensile cracks were often initiated at the tips of the joints, but the tensile cracks were initiated at the middle of the joint when β was low ($\beta = 0°$ and $\beta = 15°$ in both the 2D and 3D models) for uniaxial compression and when β reached 90° for the uniaxial tensile stress.

Author Contributions: Conceptualization, Y.Z. (Yang Zhao) and Y.Z. (Ye Zhao); methodology, Y.Z. (Yang Zhao); software, Y.Z. (Ye Zhao); validation, Y.Z. (Yang Zhao), Y.Z. (Ye Zhao) and Z.Z.; formal analysis, W.W.; investigation, J.S.; resources, Y.C.; data curation, J.N.; writing—original draft preparation, Y.Z. (Yang Zhao); writing—review and editing, Y.Z. (Yang Zhao); visualization, L.J.; supervision, L.J.; project administration, Y.Z. (Yang Zhao); funding acquisition, L.J. All authors have read and agreed to the published version of the manuscript.

Funding: This research received no external funding.

Data Availability Statement: The data used to support the results of this study can be found in this manuscript text.

Acknowledgments: This study was financially supported by the Young Scientist Project of the National Key Research and Development Program of China (Grant No. 2021YFC2900600), the National Natural Science Foundation of China (52074166) and Shandong Province (ZR2021YQ38), the Open Grant of the State Key Laboratory of Mining Response and Disaster Prevention and Control in Deep Coal Mines (SKLMRDPC20KF02), and the Shandong Energy Group Co., LTD, grant no. 2019SDZY02.

Conflicts of Interest: The authors declare that they have no known competing financial interest or personal relationship that could have appeared to influence the work reported in this paper.

References

1. Yao, W.; Xia, K.; Li, X. Non-local failure theory and two-parameter tensile strength model for semi-circular bending tests of granitic rocks. *Int. J. Rock Mech. Min. Sci.* **2018**, *110*, 9–18. [CrossRef]
2. Shu, J.; Jiang, L.; Kong, P.; Wang, Q. Numerical analysis of the mechanical behaviors of various jointed rocks under uniaxial tension loading. *Appl. Sci.* **2019**, *9*, 1824. [CrossRef]
3. Zhao, Y.; Ning, J.; Jiang, L.; Wang, Q.; Yuan, A. Numerical Analysis on the Joint Weakening Effect of Rock Mass Behaviors in Tension. *Lithosphere* **2022**, *2022*, 5324148. [CrossRef]
4. Liu, Z.G.; Chen, J.Y.; Bai, W.F.; Xu, Q. Improved parameter selection method for mesoscopic numerical simulation test of direct tensile failure of rock and concrete. *J. Cent. South Univ. Technol.* **2010**, *17*, 1079–1086. [CrossRef]
5. Zhang, Y.; Deng, H.; Deng, J.; Liu, C.; Yu, S. Peridynamic simulation of crack propagation of non-homogeneous brittle rock-like materials. *Theor. Appl. Fract. Mech.* **2020**, *106*, 102438. [CrossRef]
6. Dop, A.; Pac, B. A bonded-particle model for rock. *Int. J. Rock Mech. Min. Sci.* **2004**, *41*, 1329–1364.
7. Peng, J.; Wong LN, Y.; Teh, C.I. Effects of grain size-to-particle size ratio on micro-cracking behavior using a bonded-particle grain-based model. *Int. J. Rock Mech. Min. Sci.* **2017**, *100*, 207–217. [CrossRef]
8. Wu, Y.; Zhao, Y.; Tang, P.; Wang, W.; Jiang, L. Analysis of the mechanical properties and failure modes of rock masses with nonpersistent joint networks. *Geomech. Eng.* **2022**, *30*, 281.
9. Tong, R.; Liu, H.; Liu, J.; Shi, Y.; Xie, L.; Ban, S. Meso-Mechanical Characteristics of Granite with Natural Cracks after Mud Acid Corrosion. *Energies* **2022**, *15*, 721. [CrossRef]
10. Wang, S.; Zhou, J.; Zhang, L.; Han, Z. Numerical investigation of injection-induced fracture propagation in brittle rocks with two injection wells by a modified fluid-mechanical coupling model. *Energies* **2020**, *13*, 4718. [CrossRef]
11. Cheng, Y.; Jiao, Y.Y.; Tan, F. Numerical and experimental study on the cracking behavior of marble with En-Echelon flaws. *Rock Mech. Rock Eng.* **2019**, *52*, 4319–4338. [CrossRef]
12. Potyondy, D.O. A flat-jointed bonded-particle material for hard rock. In Proceedings of the 46th US Rock Mechanics/Geomechanics Symposium, Chicago, IL, USA, 24–27 June 2012.
13. Yang, X.X.; Qiao, W.G. Numerical investigation of the shear behavior of granite materials containing discontinuous joints by utilizing the flat-joint model. *Comput. Geotech.* **2018**, *104*, 69–80. [CrossRef]
14. Cheng, Y.; Wong, L.N.Y. A study on mechanical properties and fracturing behavior of Carrara marble with the flat-jointed model. *Int. J. Numer. Anal. Methods Geomech.* **2020**, *44*, 803–822. [CrossRef]
15. Li, X.F.; Li, H.B.; Liu, Y.Q.; Zhou, Q.C.; Xia, X. Numerical simulation of rock fragmentation mechanisms subject to wedge penetration for TBMs. *Tunn. Undergr. Space Technol.* **2016**, *53*, 96–108. [CrossRef]
16. Kong, L.; Ranjith, P.G.; Li, Q.B.; Song, Y. Rock grain-scale mechanical properties influencing hydraulic fracturing using Hydro-GBM approach. *Eng. Fract. Mech.* **2022**, *262*, 108227. [CrossRef]
17. Liu, Y.; You, Z. Accelerated discrete-element modeling of asphalt-based materials with the frequency-temperature superposition principle. *J. Eng. Mech.* **2011**, *137*, 355–365. [CrossRef]
18. Gao, L.; Zhang, Y.; Liu, Y.; Wang, Z.; Ji, X. Study on the cracking behavior of asphalt mixture by discrete element modeling with real aggregate morphology. *Constr. Build. Mater.* **2023**, *368*, 130406. [CrossRef]
19. Tahmasebinia, F.; Zhang, C.; Canbulat, I.; Vardar, O.; Saydam, S. Computing the damage and fracture energy in a coal mass based on joint density. *Int. J. Min. Sci. Technol.* **2018**, *28*, 813–817. [CrossRef]

20. Feng, Z.; Chen, X.; Fu, Y.; Qing, S.; Xie, T. Acoustic Emission Characteristics and Joint Nonlinear Mechanical Response of Rock Masses under Uniaxial Compression. *Energies* **2021**, *14*, 200. [CrossRef]
21. Zhu, C.; Karakus, M.; He, M.; Meng, Q.; Shang, J.; Wang, Y.; Yin, Q. Volumetric deformation and damage evolution of Tibet interbedded skarn under multistage constant-amplitude-cyclic loading. *Int. J. Rock Mech. Min. Sci.* **2022**, *152*, 105066. [CrossRef]
22. Wang, Y.; Yang, H.N.; Han, J.Q.; Zhu, C. Effect of rock bridge length on fracture and damage modelling in granite containing hole and fissures under cyclic uniaxial increasing-amplitude decreasing-frequency (CUIADF) loads. *Int. J. Fatigue* **2022**, *158*, 106741. [CrossRef]
23. Zhao, Y.; Wu, Y.N.; Xu, Q.; Jiang, L.S.; Huang, W.P.; Zhang, P.P.; Niu, Z.T. Numerical analysis of the mechanical behavior and failure mode of jointed rock under uniaxial tensile loading. *Adv. Civ. Eng.* **2020**, *2020*, 8811282. [CrossRef]
24. Yang, S.Q.; Jing, H.W. Evaluation on strength and deformation behavior of red sandstone under simple and complex loading paths. *Eng. Geol.* **2013**, *164*, 1–17. [CrossRef]
25. Shi, C.; Shen, J.L.; Xu, W.Y.; Wu, R.B.; Wang, W. Micromorphological characterization and random reconstruction of 3D particles based on spherical harmonic analysis. *J. Cent. South Univ.* **2017**, *24*, 1197–1206.
26. Zhao, Y.; Jiang, L.; Li, C.; Niu, Q.; Sainoki, A.; Mitri, H.S.; Ning, J. Experimental Investigation into the Mechanical Behavior of Jointed Soft Rock Using Sand Powder 3D Printing. *Rock Mech. Rock Eng.* **2023**, 1–22. [CrossRef]
27. Niu, Q.; Jiang, L.; Li, C.; Zhao, Y.; Wang, Q.; Yuan, A. Application and prospects of 3d printing in physical experiments of rock mass mechanics and engineering: Materials, methodologies and models. *Int. J. Coal Sci. Technol.* **2023**, *10*, 5. [CrossRef]
28. Kong, P.; Jiang, L.; Shu, J.; Sainoki, A.; Wang, Q. Effect of fracture heterogeneity on rock mass stability in a highly heterogeneous underground roadway. *Rock Mech. Rock Eng.* **2019**, *52*, 4547–4564.
29. Zhou, X.P.; Fu, L.; Ju, W.; Berto, F. An experimental study of the mechanical and fracturing behavior in PMMA specimen containing multiple 3D embedded flaws under uniaxial compression. *Theor. Appl. Fract. Mech.* **2019**, *101*, 207–216. [CrossRef]
30. Saksala, T. Numerical modeling of temperature effect on tensile strength of granitic rock. *Appl. Sci.* **2021**, *11*, 4407. [CrossRef]
31. Aydan, Ö. *Rock Mechanics and Rock Engineering: Volume 1: Fundamentals of Rock Mechanics*; CRC Press: Boca Raton, FL, USA, 2019.
32. Christensen, R.M. *Mechanics of Composite Materials*; Courier Corporation: Chelmsford, MA, USA, 2012.
33. Fan, W.C.; Yang, H.; Jiang, X.L.; Cao, P. Experimental and numerical investigation on crack mechanism of folded flawed rock-like material under uniaxial compression. *Eng. Geol.* **2021**, *291*, 106210.